Calibration methods for a dual-wavelength interferometer system

Yanqi Zhang[a], Martin Tangari Larrategui[a], Thomas G. Brown[a], Jonathan D. Ellis*[b]
[a]The Institute of Optics, University of Rochester, 480 Intercampus Dr, NY 14627
[b]College of Optical Sciences, University of Arizona, 1630 E. University Blvd., AZ 85721

ABSTRACT

Multiple wavelength interferometry has long been considered an option for the measurement of large aspheric slope departures. In particular, a synthetic wavelength offers a variety of approaches by which large phase excursions can be unwrapped. Using multiple wavelengths can create collimation and magnification mismatch errors between the individual wavelengths that arise during beam expansion and propagation. Here, we present and analyze alignment and calibration methods for a dual-wavelength interferometer that can significantly reduce both misalignment errors and chromatic aberrations in the system. To correct for misalignment, a general method is described for the alignment of a dual-wavelength interferometer, including the alignment of lasers, beam expanders, beam splitters for combining beams and for compensating errors in the reference surface, and the fringe imaging system. A Fourier transform test at the detector surface was conducted to validate that there is essentially no magnification difference between two wavelengths resulting from misalignment of optical system. For the chromatic aberration introduced by the optical elements in the system, a ray-trace model of the interferometer has been established, to simulate the chromatic effect that optical elements will have on the measurement results. As an experimental test, we examine an off-axis spherical mirror in a non-null condition using a highly aliased interferogram. The above alignment methods and the results are analyzed based on the simulated system errors. Using this method, we demonstrate a measured surface profile of deviation of λ/25 which is comparable to a direct measurement profile of the surface on axis using a Fizeau interferometer.

Keywords: dual-wavelength interferometry, surface metrology

1. INTRODUCTION

The wide application of aspheric surfaces and freeform surfaces has brought enormous benefits to the progress of optical technologies, reducing the size, weight, and complexity of optical systems. While the rapid development of design and fabrication technologies has offered the possibility of using steep surface slopes [1], new metrology methods are still needed because of high demand in accuracy, measurement range, and throughput. Among the various optical surface metrology methods, dual-wavelength interferometry has long been pursued as one way to increase measurement range while maintaining accuracy [2].

Dual-wavelength interferometry provides a solution for the limited resolving capability in the single wavelength interferometry [3, 4]. The equivalent wavelength synthesized from two single wavelengths is expressed by

$$\lambda_{eq} = \left| \frac{\lambda_1 \lambda_2}{\lambda_1 - \lambda_2} \right|, \tag{1}$$

where the λ_1 and λ_2 represent two single wavelengths and λ_{eq} represents the synthetic wavelength. In this way, the

*jdellis@optics.arizona.edu

measurement range can be enlarged using the longer wavelength without suffering from the specific needs for optical elements and detectors in the infrared spectrum.

Two of the major limitations of dual-wavelength interferometry are magnification error [5], and the reduced accuracy from wavelength amplification. Magnification error results from a wavelength mismatch in beam size during fringe formation at the detector surface. The difference in apparent OPD between the two wavelengths is amplified during the wavelength synthesizing process and added to the synthetic wavefront, reducing the measurement accuracy. Meanwhile, since the noise in the measurement is proportional to the source wavelength of the interferometer system, the noise is effectively amplified by using a synthetic wavelength. Figure 1 illustrates how the beam size mismatch results in an error of the measured wavefront.

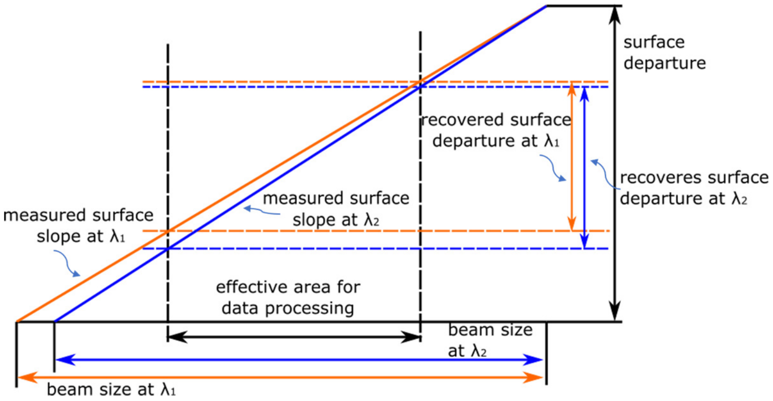

Figure 1. The relationship between the magnification and recovered surface departure.

Taking these two errors into consideration, the measured wavefront, in terms of optical path difference (OPD), is represented by

$$\begin{aligned} OPD &= \left(\frac{1}{2\pi}\right)\left(\phi_2-\phi_1+\Delta\phi_{ME}\right)\left[\frac{\lambda_{eq}}{\left(\lambda_1+\lambda_2\right)/2}\right]\left(\frac{\lambda_1+\lambda_2}{2}\right) \\ &= \left(\frac{1}{2\pi}\right)\left(\phi_2-\phi_1+\Delta\phi_{ME}\right)M\left(\frac{\lambda_1+\lambda_2}{2}\right) \end{aligned}, \quad (2)$$

where ϕ_1 and ϕ_2 represent the wavefront measured with the single wavelengths λ_1 and λ_2, and $\Delta\phi_{\mathrm{ME}}$ represents the contribution of the magnification error. Therefore, solving these intrinsic problems becomes essential to further explore the capability of dual-wavelength interferometry.

The beam size mismatch in a dual-wavelength system may arise through both system misalignment and chromatic errors. Chromatic errors contribute to a magnification error if the imaging system suffers from chromatic aberration and is not corrected at both wavelengths. Additionally, the individual sources travel through different optical paths before being combined by a beam splitter, also potentially contributing to magnification differences.

In this paper, the configuration of a dual-wavelength interferometer is described, and the general alignment methods are demonstrated. These alignment methods are also applicable to multi-wavelength systems. Then, an optical model of the interferometer system is established to simulate the chromatic errors in the system, as well as to provide a guideline for the calibration. A magnification testing method is proposed to verify that the remaining magnification errors are from the intrinsic chromatic effect instead of system misalignments. Finally, the single wavelength correction method is applied to eliminate the magnification error effect and noise amplification effect in the system. The measurement results of an off-axis spherical mirror are presented to demonstrate the feasibility of this method.

2. SYSTEM DESIGN AND ALIGNMENT

2.1 Dual-wavelength interferometer system

The interferometer design is based on a conventional Twyman-Green configuration, with the introduction of a second laser source. The output beams from two lasers are expanded and collimated individually before combined by a beam splitter. Figure 2a shows the dual-wavelength interferometer with a nominal flat surface under test. The benchtop system developed in the lab is shown in Figure 2b. In this system, laser sources of 633 nm and 594 nm are selected, generating a synthetic wavelength of 9.641 µm.

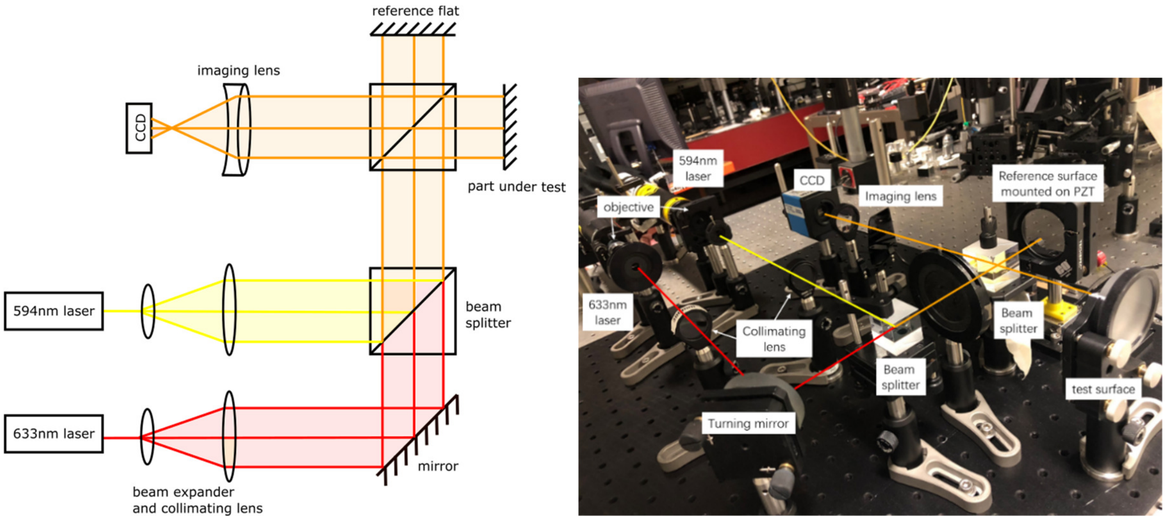

(a) (b)

Figure 2. (a) Dual-wavelength interferometer system configuration; (b) the benchtop system of the dual-wavelength interferometer.

2.2 General alignment methods

The alignment of this system was performed in the following order: the laser sources, the beam expanders and collimation lens, the beam splitter combining two laser sources, the beam splitter dividing the test and reference wavefronts, the reference surface, and the imaging system including imaging lenses and detector. The system is tested during alignment to validate the beams collimation, imaging quality, and beam size matching.

The system can be efficiently aligned with a calibration card, on which a crosshair is placed in the middle of a bull’s-eye pattern. Before alignment, the direction of optical axis is determined, usually by the alignment of screw holes on the optical table. During the alignment of each element, the calibration card is moved towards and off the element along the optical axis, to keep the center of the laser beam superimposing the crosshair. Figure 3a shows the calibration card, and Figure 3b shows the alignment of laser and turning mirror with the application of calibration card. The subsequent alignment in the aforementioned alignment order follows the same procedures.

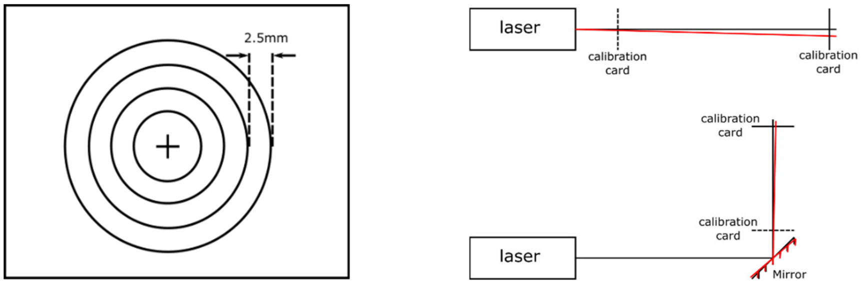

(a) (b)

Figure 3. (a) Calibration card; (b) alignment of laser source and turning mirror with calibration card.

The collimation test is required after the collimating lens is inserted and aligned in the system for each wavelength individually. A shear plate provides a visual method for collimation verification, as Figure 4 shows.

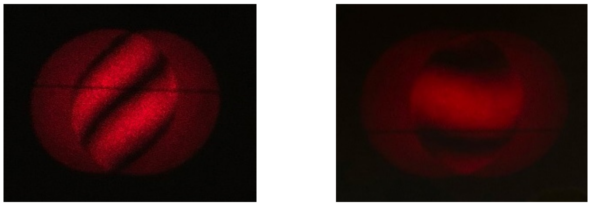

(a) (b)

Figure 4. Shear plate test of beams in (a) poor and (b) good collimating conditions.

The alignment and collimation procedure assures that the beams from two lasers follow coincident optical paths. An aperture is then placed between the two beam splitters to ensure that the incident beams have identical beam diameters.

3. MAGNIFICATION CALIBRATION

3.1 Chromatic aberration effect simulation

Chromatic aberrations introduced during propagation and imaging can, in principle, be quantified and corrected using simulation tools. Figure 5 illustrates a sequential model established using parameters measured from the benchtop system.

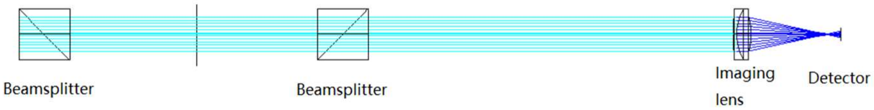

Figure 5. The optical model in sequential order.

To quantify the beam size at the detector surface, the optical path of the interferometer is unfolded to a sequential optical path and the irradiance profile is estimated using a spot diagram. In this case, the fields angles range from 0 to 0.5 degree to simulate the local tilt of a surface under test. Figure 6 shows the spot diagrams at both wavelengths.

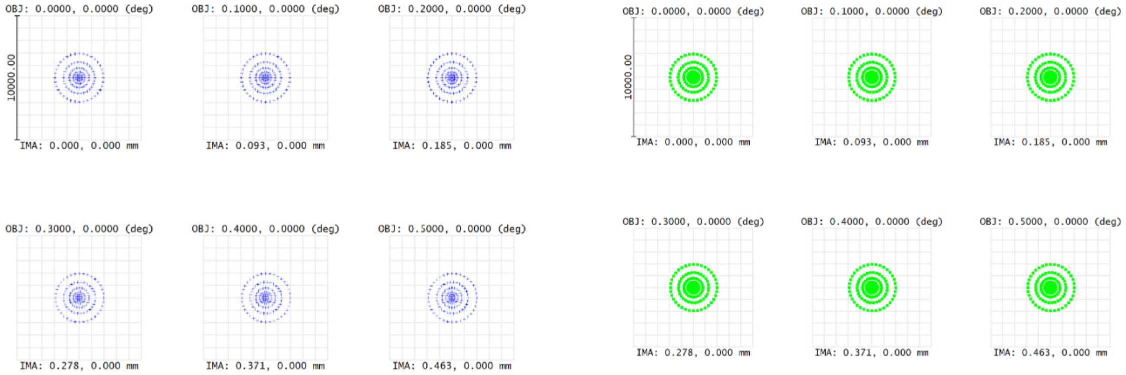

(a) (b)

Figure 6. Spot diagrams at wavelengths of (a) 633 nm and (b) 594 nm

The RMS beam radius on the imaging surface is calculated for each field angle and wavelength, as shown in Table 1. The magnification factor (defined by the magnification ratio between two wavelengths) is then estimated by the ratio of beam sizes. According to the table, the magnification error does increase with the field of view, but the change is small when compared to the field-independent error. The value of the magnification factor can therefore be treated as a field-independent constant value of 0.99677.

Table 1. The RMS radius of beam spot corresponding to difference fields and wavelengths.

FOV /[degree]	0	0.1	0.2	0.3	0.4	0.5
RMS Radius at 633 nm / [μm]	1270.19	1270.24	1270.38	1270.62	1270.95	1271.38
RMS Radius at 594 nm / [μm]	1274.30	1274.35	1274.49	1274.73	1275.06	1275.49
Magnification factor	0.996775	0.996775	0.996775	0.996776	0.996777	0.996778

3.2 Magnification matching test

To experimentally test the simulation, a tilted flat was used as the surface under test. Since we know that the test surface shape must be the same for both wavelengths, the number of fringes on the sensor should be inversely proportional to the wavelength. Assuming a fringe spacing of d_1 for λ_1 and d_2 for λ_2, the relationship between fringe period and wavelength is expressed in the following equation, under the circumstance that there is no magnification error:

$$\frac{d_1}{d_2}=\frac{\lambda_1}{\lambda_2}\,. \tag{3}$$

When considering the beam size mismatch,

$$\frac{d_1'}{d_2'}=M\frac{d_1}{d_2}=M\frac{\lambda_1}{\lambda_2}\,, \tag{4}$$

in which d_1' and d_2' indicate the fringe spacings at two individual wavelengths with magnification error in the system. In Equation 4, M represents the magnification factor between two wavelengths. From the interferogram, a sinusoidal function can be extracted across the perpendicular direction of the fringes. By applying a Fourier transform to the sinusoidal functions, as shown in Figure 7, the ratio of fringe spacings d_1' and d_2' is represented by the distance between the sidelobe and the origin in frequency domain as,

$$\frac{d_1'}{d_2'} = \frac{D_2}{D_1} = M\frac{\lambda_1}{\lambda_2}. \tag{5}$$

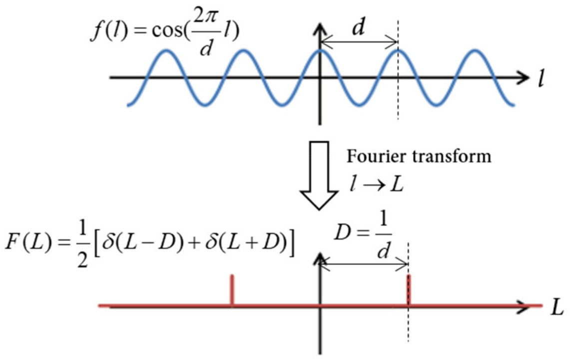

Figure 7. The Fourier transform of a cosine function in the frequency domain [6].

Figure 8 shows the interferograms with tilted flat under test at both wavelengths. Figure 9 shows the Fourier transform of the interferogram. With quadratic interpolation of sinusoidal peaks [7], the location of the central peak L_0 and the side lobes L_{633} and L_{594} can be determined. Following Equation 5, the magnification factor is acquired as M=0.9967, which verifies the simulation results in Section 3.1. Therefore, the magnification error on detector surface is demonstrated to be from the chromatic aberration introduced by the optical elements after the aperture.

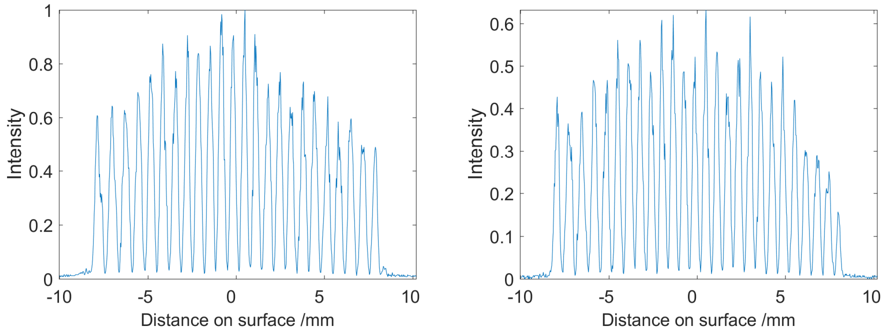

(a) (b)

Figure 8. Interferograms of the tilted flat at (a) 633 nm and (b) 594 nm.

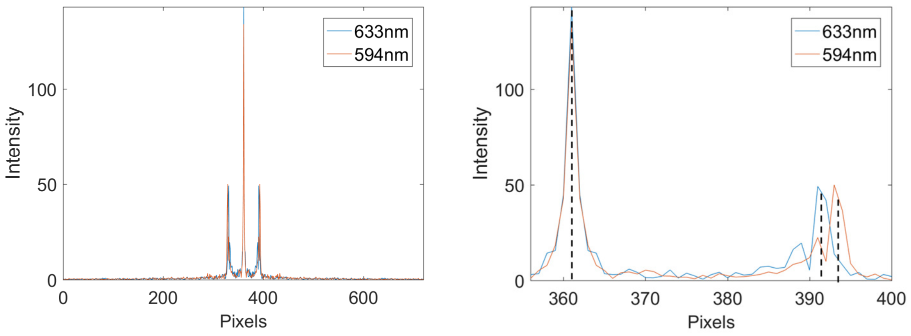

(a) (b)

Figure 9. The Fourier transform of the interferogram with (a) full scale and (b) magnified view on the central peak and side lobes.

3.3 Single wavelength correction method

Even though the fine alignment of the system mitigates the effect of beam size mismatch, chromatic aberrations are inevitable from the presence of optical elements. Therefore, a data processing method for synthesizing wavelengths is applied to solve the remaining magnification errors and amplified noises. Creath [8, 9] has described a single wavelength correction method that uses the intact wavefront information of the synthetic wavelength with no unwrapping ambiguities, to correct the unwrapped wavefronts of single wavelengths with the unwrapping errors. By conducting a pixel-by-pixel comparison of the wavefronts between equivalent wavelength and single wavelength, an integer number of 2π is added or subtracted to the single wavelength phase map, where there is a phase difference. This method is only applicable when the noise of synthetic wavelength wavefront is less than $\lambda/4$, where λ indicates the single wavelength to be corrected.

The major problem of this method is that the synthetic wavefront deviates from actual surface figure due to the magnification error, therefore is not accurate to be considered as the reference for correction. If there is no magnification error, the wavefronts at the synthetic wavelength and the single wavelength have the same slope departure (Figure 10a). By conducting the single wavelength correction method mentioned above, the unwrapping ambiguities can be removed in the single wavelength interferometry. If there is a deviation between two wavefronts (Figure 10b), in the wavefront after correction, the slope at each pixel keeps original as wavefront at single wavelength, while the phase value is corrected to be the same as wavefront at synthetic wavelength. After removing the continuous wavefront from corrected wavefront, the residual pattern is a wrapped surface with the height equal to single wavelength (Figure 10c).

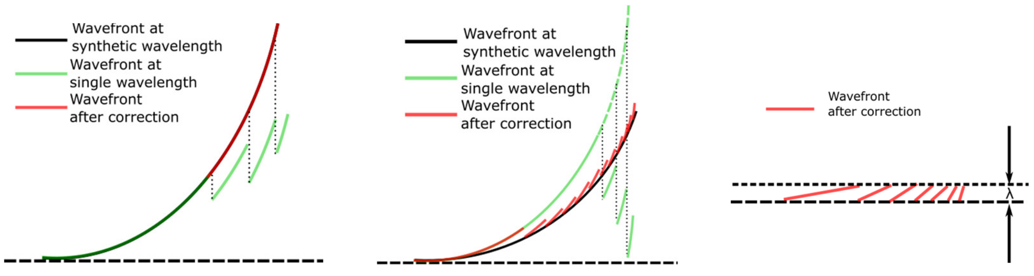

(a) (b) (c)

Figure 10. (a) Wavefront correction without magnification error; (b) wavefront correction with magnification error; (c) corrected wavefront after removing the continuous wavefront.

Therefore, a modified single wavelength correction method is proposed to correct the unwrapping ambiguities without being affected by magnification error, as shown in Figure 11. The corrected wavefront is fitted to a Zernike polynomial to identify the continuous surface that can be removed from the wavefront. The residual pattern is then unwrapped, representing the wavefront deviation between synthetic and single wavelengths. The final corrected wavefront is acquired by combining the wavefront after first correction, and the wavefront deviation.

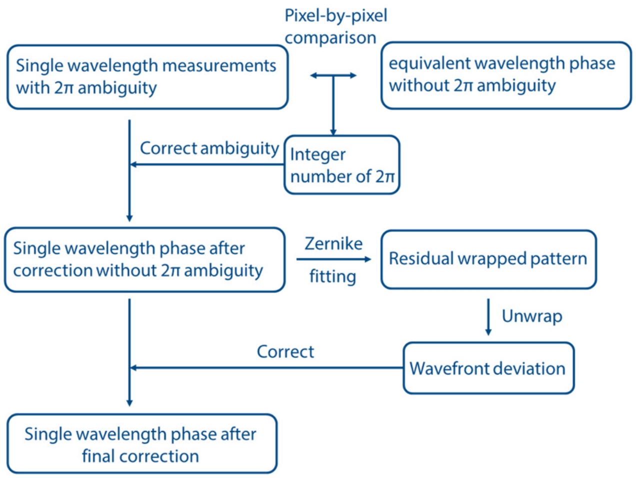

Figure 11. Flow chart describing the modified single wavelength correction method.

4. EXPERIMENTAL RESULTS AND ANALYSIS

Using the interferometer described in Section 2.1, a tilted spherical mirror was introduced in the test arm in a non-null configuration (*i.e.*, without a reference sphere), to generate highly aliased interferograms that cannot be resolved by conventional single wavelength interferometry. A closed-loop piezo stage was used for phase shifting at individual wavelengths, and a six-step least-squared algorithm was used for phase extraction. The interferograms for each wavelength were recorded after each step. Figure 12 shows an example of an aliased interferogram recorded at 633 nm, in which the top of the interferogram shows a low visibility aliasing pattern.

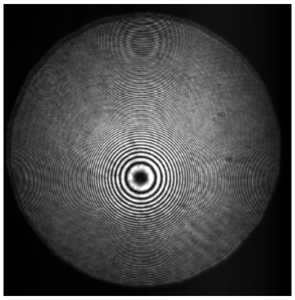

Figure 12. Interferogram at 633 nm. The interference fringes are aliased at the edge of the surface.

Figure 13 shows the extracted phase maps at 633 nm and 594 nm respectively. Figure 14 shows the unwrapped surface figure using the phase maps. The discontinuities in the unwrapped surface illustrate the failure of single wavelength interferometry for large slope departures.

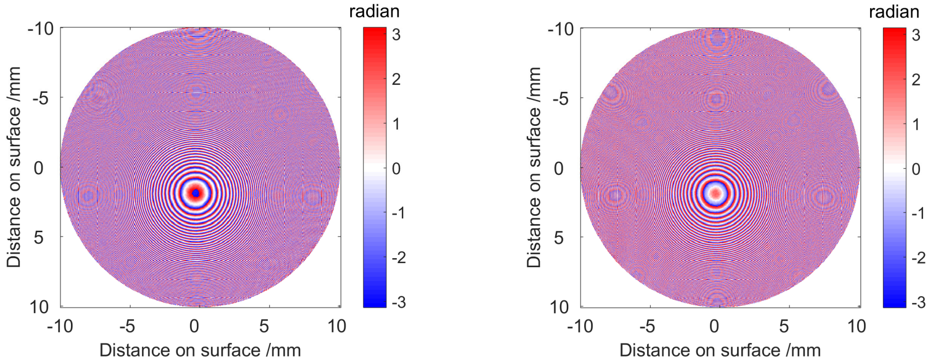

(a)

(b)

Figure 13. The extracted phase map at (a) 633 nm and (b) 594 nm

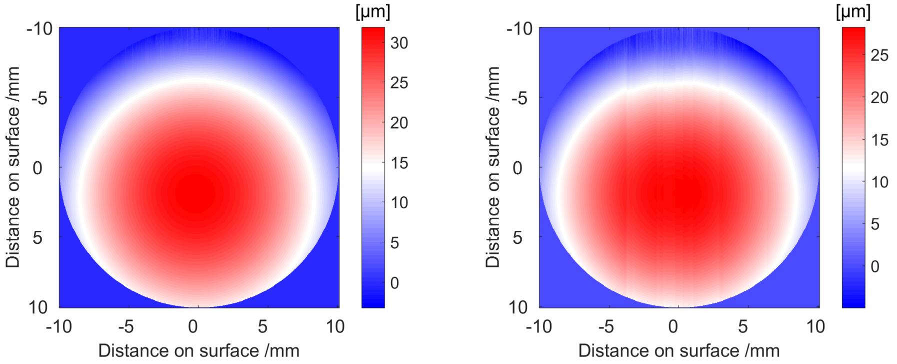

(a)

(b)

Figure 14. The unwrapped surface figure at (a) 633 nm and (b) 594 nm

The phase map formed by the synthetic wavelength over an equivalent aperture (‘effective area’) is illustrated in Figure 15a. The aliased area in the single wavelength phase map has been eliminated using the synthetic wavelength, at the cost of noise amplification. Figure 15b shows the unwrapped surface figure from the synthetic phase map.

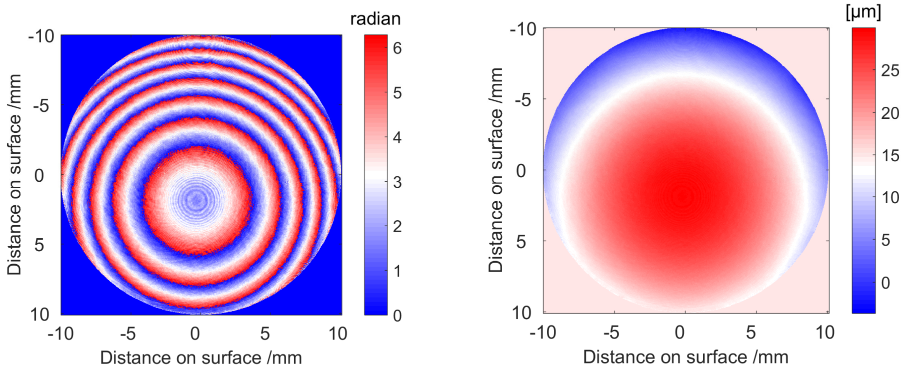

(a) (b)

Figure 15. (a) The synthetic phase map at the equivalent wavelength of 9.641 μm; (b) the unwrapped surface figure at synthetic wavelength.

The unwrapped surface figure at the synthetic wavelength is then applied to the single wavelength phase map to correct residual discontinuities. The correction process applied to a measurement at 633 nm is demonstrated here. Following the flow chart in Figure *11*, the difference between the unwrapped surface figure at a wavelength of 633 nm and the synthetic wavelength is calculated, as shown in Figure 16a. From this difference map, the number of multiples of 2π is determined, to be added or subtracted to the single wavelength wavefront, as shown in Figure 16b.

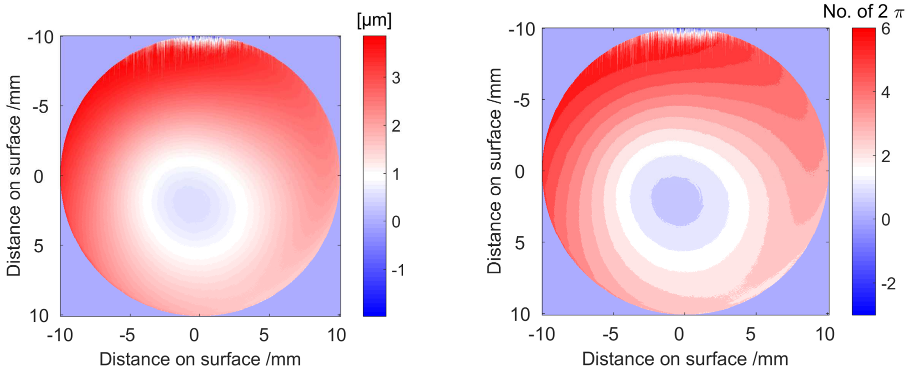

(a) (b)

Figure 16. (a) The surface figure difference between 633 nm and synthetic wavelength; (b) integer number of 2π in surface figure difference.

After correction, the 2π ambiguity is eliminated from the original unwrapped wavefront, as shown in Figure 17a. To assess the corrected result, the surface after correction is fitted with Zernike polynomials using the first 25 terms. Figure 17b shows the reconstructed wavefront with the fitted coefficients, which eliminates the unwrapping errors in the single wavelength interferometry results. The residual pattern after removing the reconstructed wavefront is shown in Figure 17c.

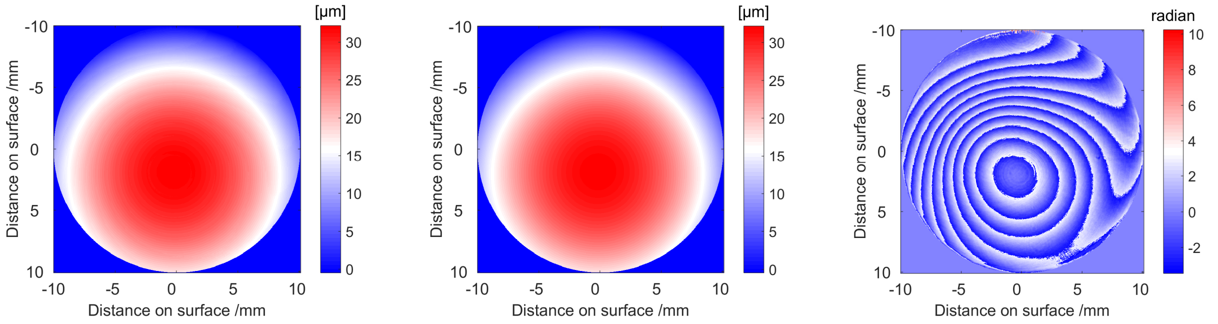

(a) (b) (c)

Figure 17. (a) Surface figure at 633 nm after correction; (b) reconstructed surface from the corrected surface at 633 nm; (c) residual after removing reconstructed surface form corrected surface.

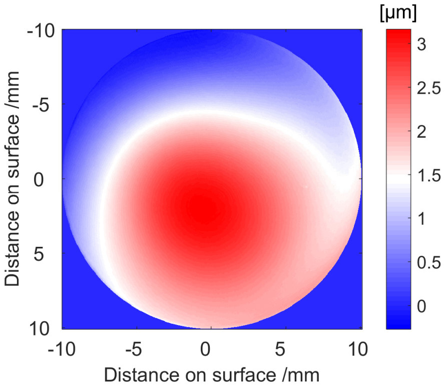

Figure 18. The deviation between wavefronts at the synthetic and the single wavelengths.

The wavefront deviation is unwrapped from the residual pattern, as shown in Figure 18. Figure 19a shows the surface figure at 633 nm after correction. In the same procedure, the surface figure at wavelength of 594 nm is recovered, as shown in Figure 19b.

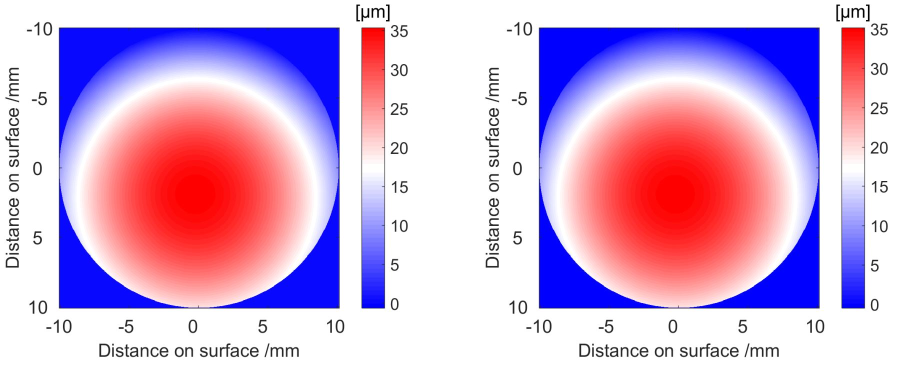

(a) (b)

Figure 19. Corrected surface with the single wavelength correction method at the wavelength of (a) 633 nm and (b) 594 nm.

By comparing the surfaces after correction (Figure 19), and the directly unwrapped surfaces which have 2π ambiguities

(Figure 14), the differences are shown in Figure 20. Figure 20 indicates that the surfaces after correction keep original surface information such as tilt and surface power in the single wavelength measurement, since differences between corrected and uncorrected surface are constants in the area without 2π ambiguities. Meanwhile, the surface after correction also demonstrates that this method keeps the enlarged measurement range from synthetic wavelength.

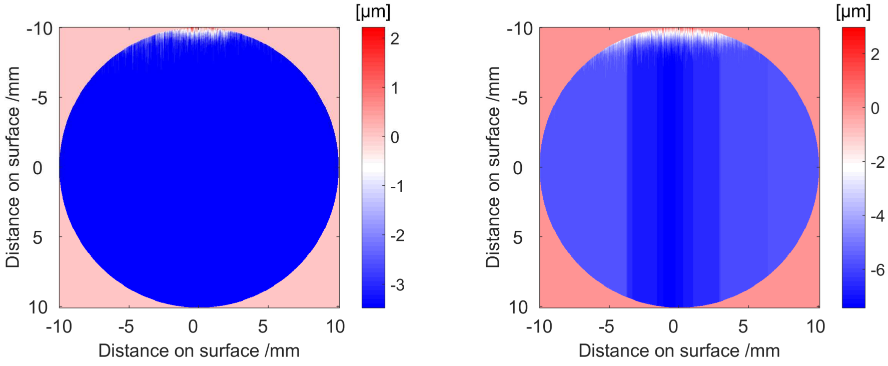

(a) (b)

Figure 20. Difference between the corrected and uncorrected surfaces at the wavelength of (a) 633 nm and (b) 594 nm.

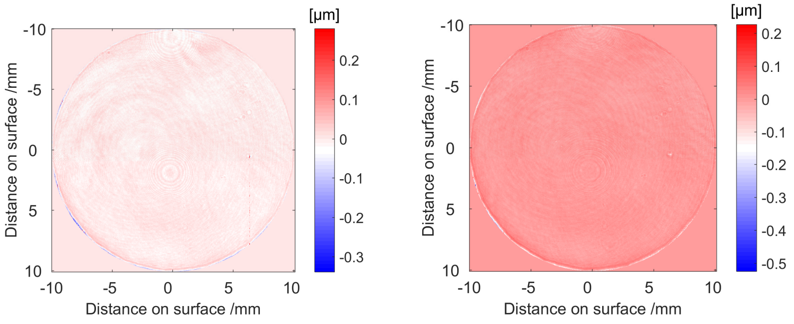

(a) (b)

Figure 21. Residual after removing reconstructed surface from the measured surface at wavelength of (a) 633 nm and (b) 594 nm.

Figure 21 shows the surfaces after removing the reconstructed surface which uses the first 25 terms in Zernike polynomial, from the measured surface figure, at both single wavelengths. The RMS of residual surface is calculated to be 0.0244 μm for wavelength of 633 nm and 0.0228 μm for wavelength of 594 nm, equivalent to approximately λ/25.

5. CONCLUSION

We have presented, and experimentally tested, correction schemes for large slope departures measured in a dual-wavelength Twyman-Green interferometer. This system uses synthetic wavelength interferometry to unwrap highly aliased interferograms while correcting for magnification errors and other chromatic aberrations. We described general alignment methods for the system, including beam pointing, collimation and imaging, with special consideration given to the challenges of a multi-wavelength systems. This alignment method is paired with an optical model of the system to guide the alignments. An off-axis spherical mirror was measured and compared to an optical flat reference, generating highly aliased fringes, to demonstrate the feasibility of this technique.

ACKNOWLEDGEMENT

The authors would like to thank the Center for Freeform Optics (CeFO) under NSF:IIP: 1338877 and NSF:CMMI 1653510 for financial support of this work.

REFERENCES

[1] D. M. C. N. E. Claytor, et al, “An overview of freeform optics production,” Proceeding of ASPE winter topical meeting, (2004).

[2] Y. Y. Cheng, and J. C. Wyant, “2-Wavelength Phase-Shifting Interferometry,” Applied Optics, 23(24), 4539-4543 (1984).

[3] M. North-Morris, [Test and Measurement: Multiple-wavelength interferometry measures large segmetned mirrors], (2005).

[4] D. Malacara, [Optical Shop Testing (Wiley Series in Pure and Applied Optics)] Wiley-Interscience, (2007).

[5] J. C. Wyant, “Testing Aspherics with 2-Wavelength Holography,” Journal of the Optical Society of America, 61(5), 655-& (1971).

[6] BobP, [Fourier Transform of a sin(2pi*x)], (2015).

[7] J. O.Smith, [Quadratic Interpolation of Spectral Peaks] W3K, (2011).

[8] K. Creath, [Measuring Step Heights Using An Optical Profiler], (1986).

[9] K. Creath, and J. C. Wyant, "Direct Phase Measurement Of Aspheric Surface Contours." 0645, 6.